

# Vortex phase diagram in $\text{Bi}_2\text{Sr}_2\text{CaCu}_2\text{O}_{8+\delta}$ with damage tracks created by 30 MeV fullerene irradiation

N. ISHIKAWA<sup>1,2</sup>, C.J. VAN DER BEEK<sup>1\*</sup>, A. DUNLOP<sup>1</sup>, G. JASKIEROWICZ<sup>1</sup>, MING LI<sup>3\*\*</sup>, P.H. KES<sup>3</sup>, S. DELLA-NEGRA<sup>4</sup>

<sup>1</sup>Laboratoire des Solides Irradiés, CNRS UMR 7642 & CEA/DSM/DRECAM,  
Ecole Polytechnique, 91128 Palaiseau, France

<sup>2</sup>Department of Materials Science, Japan Atomic Energy Research Institute, Tokai-mura, Ibaraki 319-1195, Japan

<sup>3</sup>Kamerlingh Onnes Laboratorium, Leiden University, P.O. Box 9506, 2300 RA Leiden, the Netherlands

<sup>4</sup>Institut de Physique Nucléaire, CNRS-IN2P3, 91406 Orsay, France

(Received )

Using 30 MeV  $\text{C}_{60}$  fullerene irradiation, we have produced latent tracks of diameter 20 nm and length 200 nm, near the surface of single crystalline  $\text{Bi}_2\text{Sr}_2\text{CaCu}_2\text{O}_{8+\delta}$ . A preliminary transmission electron microscopy study shows evidence for a very high density of deposited energy, and the ejection of material from the track core in very thin specimens. The latent tracks reveal themselves to be exceptionally strong pinning centers for vortices in the superconducting mixed state. Both the critical current density and magnetic irreversibility line are significantly enhanced. The irradiated crystals present salient features of the  $(B, T)$  phase diagram of vortex matter *both* of pristine crystals, such as the first order vortex phase transition, *and* the exponential Bose-glass line characteristic of heavy ion-irradiated crystals. We show that the latter is manifestly independent of the pinning potential.

KEYWORDS: Vortex, flux pinning, layered superconductor, latent tracks, columnar defects, phase diagram

## §1. Introduction

The recent discovery that a moderate amount of columnar strong pinning centers, induced by heavy ion irradiation,<sup>1,2</sup> does not qualitatively affect the  $(B, T)$  phase diagram of the layered superconductor  $\text{Bi}_2\text{Sr}_2\text{CaCu}_2\text{O}_{8+\delta}$ <sup>3</sup> has revived interest in disorder effects on the thermodynamics of superconductors in a magnetic field.<sup>4,5</sup> In the absence of disorder, the phase diagram is characterized by a single First Order Transition (FOT)<sup>6</sup> from an ordered vortex Bragg glass,<sup>7</sup> with both topological long range order, and long range order of the superconducting phase, to a vortex liquid that lacks either.<sup>8</sup> This low field “vortex solid” has the dynamic properties of a true superconductor, with diverging flux creep activation barriers<sup>9,10</sup> and vanishing linear resistivity, while in the vortex liquid the superconductor obeys Ohm’s law. Banerjee et al. showed that  $\text{Bi}_2\text{Sr}_2\text{CaCu}_2\text{O}_{8+\delta}$  crystals with a sufficiently small density of amorphous columnar defects still show a FOT to the vortex liquid.<sup>3</sup> A companion study by Menghini *et al.* demonstrated that in the same crystals, the vortex solid is highly disordered.<sup>11</sup> For fields below the “matching field”  $B_\phi = n_d\Phi_0$ , where  $n_d$  is the areal density of defects and  $\Phi_0 = h/2e$  is the flux quantum, vortices adapt themselves optimally to the defect positions and Bragg glass order is completely destroyed. Thus, translational symmetry of the low-field vortex lattice does not seem to be a prerequisite for the FOT.

The irrelevance of Bragg glass order can be understood by the fact that vortex tilt is what limits thermal vortex excursions near the transition.<sup>12</sup> The difference in free energy of the Bragg glass and the vortex liquid is, for sufficiently low fields, essentially determined by the difference in vortex tilt modes between the low field phase, with well-defined (disentangled) vortex lines, and the vortex liquid in which vortices are entangled. The inclusion of correlated disorder unambiguously increases pancake vortex correlations along the field direction in the vortex liquid.<sup>13–19</sup> Apparently, vortex fluctuations are also affected, as evidenced by the increase of the FOT field<sup>3</sup> and its eventual transformation into a second order Bose-glass transition.<sup>20–22</sup> Nevertheless, in the portion of the  $(B, T)$  phase diagram that is transformed from vortex liquid to Bose glass by correlated disorder, the vortices show dynamical properties reminiscent of a two-dimensional (2D) system; also, the position of the Bose-glass to liquid transition in layered superconductors is well described if one considers the system to be essentially 2D with weak coupling between layers.<sup>20</sup> The properties of the columnar defects, such as their size or density, were predicted to little affect the phase diagram of the irradiated superconductor, or the dynamical properties of the vortices.<sup>20</sup>

Here, we report on the creation of large diameter ( 20 nm ) columnar defects in optimally doped single crystalline  $\text{Bi}_2\text{Sr}_2\text{CaCu}_2\text{O}_{8+\delta}$  by 30 MeV  $\text{C}_{60}$  irradiation. A preliminary Transmission Electron Microscopy study confirms the presence of latent tracks, as well as their size distribution. The large track diameter is due to the very high energy density deposited by the fullerene fragments

\* Email address : kees.vanderbeek@polytechnique.fr

\*\* present address : Philips Semiconductors, Gerstweg 2, 6534 AE Nijmegen, the Netherlands

in the  $\text{Bi}_2\text{Sr}_2\text{CaCu}_2\text{O}_{8+\delta}$  matrix,  $S_e = 70 \text{ keVnm}^{-1}$ . The relatively small velocity of the  $\text{C}_{60}$  fragments imply the tracks are very short (an estimated 200 nm) in comparison to the thickness of usual  $\text{Bi}_2\text{Sr}_2\text{CaCu}_2\text{O}_{8+\delta}$  single crystals. The defect potential experienced by vortex lines in the mixed state is thus intermediate between that of surface damage and columnar tracks. Magneto-optical observations of the flux density on both sides of a  $40 \mu\text{m}$  thick single crystal are used to measure the critical current density and the current-voltage characteristics resulting from vortex pinning by the tracks. The creation of a random distribution of very strong pinning centers at one crystal surface only is reminiscent of Ref.<sup>23)</sup> Those authors deposited an ordered array of moderately strong pinning Fe particles on one surface of clean  $\text{Bi}_2\text{Sr}_2\text{CaCu}_2\text{O}_{8+\delta}$  single crystals of different thicknesses by means of Bitter decoration of the vortex Bragg glass. From their results, we expect vortex Bragg glass (translational) order to be destroyed only at the irradiated surface. Nevertheless, Differential Magneto-Optical (DMO) Imaging (see below) shows that the first order vortex lattice transition is preserved. Upon increasing temperature or field, the vortex solid transits, at high temperature, to a vortex liquid, and at lower temperature, to a pinned, presumably glassy phase. The temperature at which this glass transits to the vortex liquid is the same as the Bose-glass temperature in heavy-ion irradiated  $\text{Bi}_2\text{Sr}_2\text{CaCu}_2\text{O}_{8+\delta}$  crystals,<sup>20)</sup> demonstrating that the larger pinning energy expected for the  $\text{C}_{60}$ -tracks does not influence its position.

## §2. Crystal growth and irradiation procedure

$\text{Bi}_2\text{Sr}_2\text{CaCu}_2\text{O}_{8+\delta}$  single crystals were grown using the travelling-solvent floating zone method at the FOM-ALMOS center (University of Amsterdam, the Netherlands), in 200 mbar oxygen partial pressure.<sup>25)</sup> The crystals were extracted from the boule using a razor blade, and annealed in air for two weeks at  $800 \text{ }^\circ\text{C}$ . A suitable specimen, of dimensions  $980 \times 800 \times 20 \mu\text{m}^2$ , without macroscopic defects such as grain boundaries or second-phase intergrowths, was selected for further measurements using magneto-optical imaging. Some of the crystal's physical properties, such as  $T_c = 89 \text{ K}$ , characteristic for optimally doped  $\text{Bi}_2\text{Sr}_2\text{CaCu}_2\text{O}_{8+\delta}$ , the vortex lattice FOT field at low temperature ("second peak field"),<sup>26)</sup>  $B_{FOT} = 300 \pm 10 \text{ G}$ , and the low temperature  $I(V)$  characteristic, were also determined before the irradiation experiment.

A number of other crystals from the same batch were finely ground to get thin fragments, and were placed on a 3 mm diameter copper grid covered with a very thin amorphous carbon film for Transmission Electron Microscopy (TEM) studies. All samples were subsequently irradiated with 30 MeV  $\text{C}_{60}$  fullerene ions, at normal incidence and at room temperature, in the tandem accelerator of the "Institut de Physique Nucléaire" at Orsay University (Orsay, France). The samples were irradiated up to a fluence of  $1 \times 10^{10} \text{ molecules} \cdot \text{cm}^{-2}$ . For the crystal used in the magneto-optical measurements, the track density, obtained from TEM corresponds to the  $\text{C}_{60}$ -fluence and to the matching field  $B_\phi = 0.2 \text{ T}$ . Af-

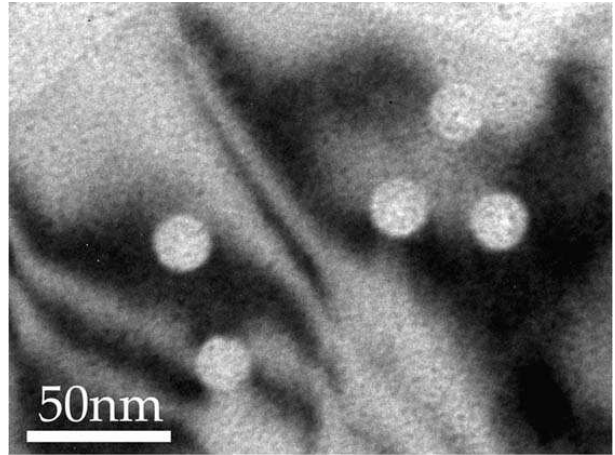


Fig. 1. Bright field image of tracks induced in  $\text{Bi}_2\text{Sr}_2\text{CaCu}_2\text{O}_{8+\delta}$  irradiated at normal incidence and at 300 K with 30 MeV  $\text{C}_{60}$  fullerenes up to a fluence of  $10^{10} \text{ cm}^{-2}$ .

ter the irradiation, the crystal retained its initial critical temperature,  $T_c = 89.0 \text{ K}$ .

## §3. Transmission electron microscopy study

### 3.1 Experimental observations

The samples destined for TEM studies were examined with a Philips CM 30 transmission electron microscope (TEM) operating at 300 kV. Since tracks created in  $\text{Bi}_2\text{Sr}_2\text{CaCu}_2\text{O}_{8+\delta}$  are rather unstable under electron irradiation, the beam current in the TEM was maintained at a low level in order to minimize the change of track structure during observation. The energy losses and the range of  $\text{C}_{60}$  clusters were calculated using the TRIM code,<sup>27)</sup> supposing that the energy loss of the cluster is the sum of the contributions of each constituent, *i.e.* here as sixty times the energy loss of individual carbon atoms of the same velocity. This additive rule is verified by a

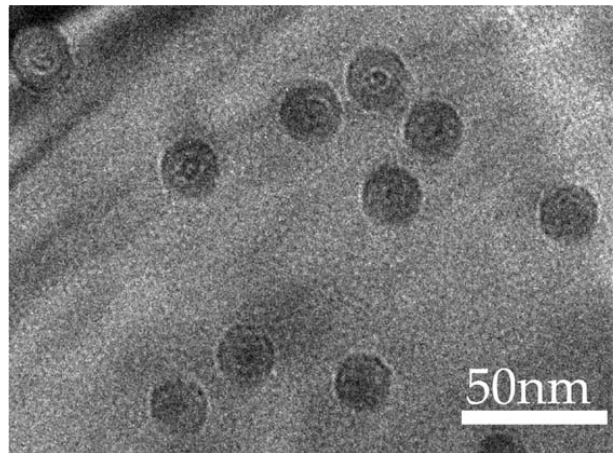


Fig. 2. Bright field image of tracks induced in  $\text{Bi}_2\text{Sr}_2\text{CaCu}_2\text{O}_{8+\delta}$  irradiated at normal incidence and at 300 K with 30 MeV  $\text{C}_{60}$  fullerenes up to a fluence of  $10^{10} \text{ cm}^{-2}$  (no reflection is excited, slight defocus of the objective lens).

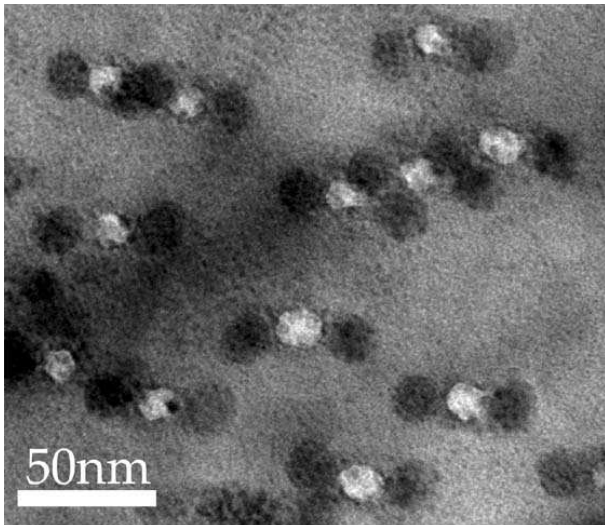


Fig. 3. Bright field image of tracks induced in very thin ( $\leq 50$  nm) regions of  $\text{Bi}_2\text{Sr}_2\text{CaCu}_2\text{O}_{8+\delta}$  irradiated at normal incidence and at 300 K with 30 MeV  $C_{60}$  fullerenes up to a fluence of  $10^{10}$   $\text{cm}^{-2}$ . The sample was tilted in the microscope by  $30^\circ$ .

number of experimental measurements of energy losses of various cluster ions.<sup>28–30</sup>) For 30 MeV fullerene ions slowing down in  $\text{Bi}_2\text{Sr}_2\text{CaCu}_2\text{O}_{8+\delta}$  we find a linear rate of energy deposition in electronic processes  $S_e = (dE/dx)_e = 69.7$   $\text{keVnm}^{-1}$ . The low incident velocity of the cluster and the lateral straggling of the projectile constituents<sup>31</sup>) lead to a rapid decrease of the linear rate of energy deposition in electronic processes by spatially correlated fragments. A comparison with previous results in other materials<sup>32</sup>) suggests that the energy deposition could fall below the threshold for the creation of latent tracks at a depth of approximately 200 nm.

The main result of this preliminary electron microscopy work is that large diameter tracks are observed. Figures 1 and 2 show bright field images of tracks in  $\text{Bi}_2\text{Sr}_2\text{CaCu}_2\text{O}_{8+\delta}$  irradiated with 30 MeV  $C_{60}$  at normal incidence. In Fig. 1 the cross-section of the tracks gives rise to a strong contrast. Namely, the regions located in the vicinity of the projectile trajectories are highly damaged, so that they diffract very differently from the surrounding matrix and give uniform white contrasts. In Fig. 2, taken in different imaging conditions (no reflection is excited, slight defocus of the objective lens), the contrast is not uniform: Fresnel fringes circle the regions corresponding to local variations of the mass thickness of the target (local thickness multiplied by the density of the material<sup>33,34</sup>). We now find an outer contrast of the same diameter as that seen in Fig. 1 and an inner contrast of a smaller diameter corresponding to the projection in the sample thickness of a different type of “object” located on the track axis. Figures 3 and 4 show bright field images of irradiated samples that have been tilted by  $30^\circ$  in the electron microscope relative to the incident ion direction. Figure 3 was taken in a very thin sample region, close to the sample edge, and shows pairs of circular black contrasts located on both sample sur-

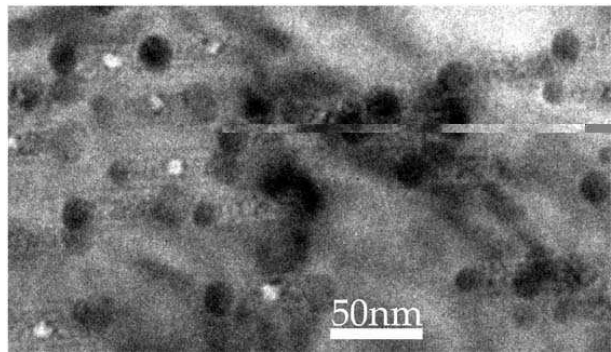


Fig. 4. Bright field image of tracks induced in  $\text{Bi}_2\text{Sr}_2\text{CaCu}_2\text{O}_{8+\delta}$  irradiated at normal incidence and at 300 K with 30 MeV  $C_{60}$  fullerenes up to a fluence of  $10^{10}$   $\text{cm}^{-2}$ . The sample was tilted in the microscope by  $30^\circ$ . The sample thickness increases from left to right. No white contrast in the center of the tracks is observed in regions thicker than  $\approx 130$  nm.

faces at the entrance and exit points of the  $C_{60}$  projectiles. A circular white contrast is found between the areas of black contrast. Figure 4 corresponds to a thicker region of the same sample (the sample thickness increases when going from the left to the right on Fig. 4), so that the projected distance between the two black contrasts is much larger than in Fig. 3. On the left part of Fig. 4, a circular white contrast is observed on the track axis approximately halfway between the projectile entrance and exit points. The diameter of the areas of white contrast is slightly smaller than the track diameter. On the right part of Fig. 4, corresponding to even thicker sample regions, the black contrasts at both track ends are still visible, but the central white contrasts are no longer there. It is difficult to define a precise thickness threshold for the creation of white objects: the areas of white contrast are imaged in regions of thickness up to about 130 nm.

### 3.2 Evolution of the track diameter

The measured diameters of the tracks generated in  $\text{Bi}_2\text{Sr}_2\text{CaCu}_2\text{O}_{8+\delta}$  by 30 MeV  $C_{60}$  fullerenes are plotted in Fig. 5. The mean diameter is estimated to be  $D = 19.7$  nm supposing that the size distribution follows a Gaussian distribution. Numerous observations by transmission electron microscopy of tracks created in  $\text{Bi}_2\text{Sr}_2\text{CaCu}_2\text{O}_{8+\delta}$  by monoatomic energetic heavy ions (Cu to U, energies of 100 MeV to 3 GeV) have been reported in the literature.<sup>35–40</sup>) The tracks were found to be amorphous with diameters in the range 3 – 16 nm. All these results have been plotted in Fig. 6, which shows the evolution of the track diameter determined by TEM as a function of the linear rate of energy deposition in electronic processes  $S_e$ . The data points lie on two different branches relative to “high velocity” and “low velocity” projectiles, referring to the fact that the corresponding ion velocity is associated to a point respectively located above or below the maximum (Bragg peak) in the slowing-down curve. This fact that at the same  $S_e$  the diameters for low-velocity mono-atomic ions are larger

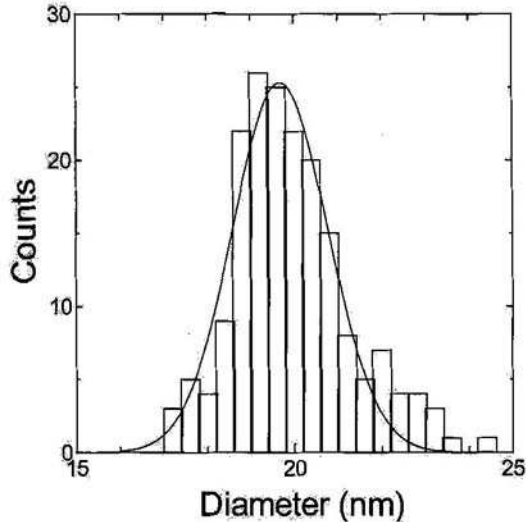


Fig. 5. Size distribution of tracks observed for  $\text{Bi}_2\text{Sr}_2\text{CaCu}_2\text{O}_{8+\delta}$  irradiated at 300 K with 30 MeV  $\text{C}_{60}$  fullerenes. The line in the figure is drawn following a Gaussian distribution.

than those for high-velocity mono-atomic ions, called in the literature the “velocity effect”, was already observed in various target types.<sup>41–43</sup> These results confirm once more that not only  $S_e$  but also the ion velocity must be taken into account to describe track formation. 30 MeV fullerene ions deposit a high rate of energy in electronic processes during their slowing-down due to the addition of the effect of each atom in the cluster. However, as they are slow projectiles ( $v/c \approx 0.01$ ), the energy of the ejected  $\delta$ -electrons is very low, so that the energy is deposited in a very close vicinity of the projectile path, leading to very high energy densities. Thus very strong structural modifications are expected. In Fig. 6, the diameter associated to cluster ions is higher than any measured using monoatomic ions and lies on the “low velocity” branch as could be expected.

### 3.3 Ejection of material from the track core

The white contrast areas (Figs. 3 and 4) correspond to regions of mass thickness lower than that of the surrounding matter, whereas the areas of black contrast most likely correspond to regions that are locally thicker. The formation of such features can be explained as follows. Just after the passage of the projectile, the excited energy density around the projectile path is very high. The excess energy can relax either radially or along the track axis. If the sample is thin, *i.e.* if both surfaces are not too far from the center of the track, matter can be expelled along the track axis and ejected. This leads to the creation of regions of very low atomic density in the center of the track, which correspond to the white contrast. If the sample thickness is too large, this process cannot occur. Some of the expelled matter stays at both track ends and forms locally thicker regions, which are subsequently observed as black contrasts at the entrance and the exit points of the projectile. As far as

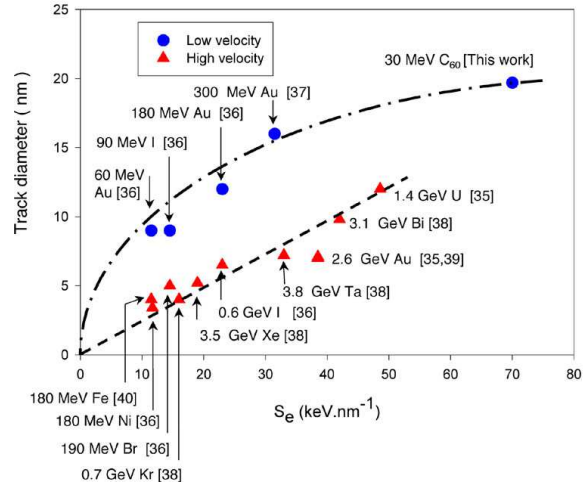


Fig. 6. Track diameters measured in  $\text{Bi}_2\text{Sr}_2\text{CaCu}_2\text{O}_{8+\delta}$  irradiated with monoatomic ions (from refs.<sup>35–40</sup>) plotted as a function of the electronic stopping power  $S_e$  for irradiations. The circles and triangles respectively correspond to the low velocity and high velocity projectiles. Our relative to 30 MeV  $\text{C}_{60}$  ions has been added (last point on the low velocity branch).

we know, similar areas of white contrast inside a damage track have never been reported for monoatomic ion irradiation. Note that a very similar result has previously been observed in insulating  $\text{Y}_3\text{Fe}_5\text{O}_{12}$  garnet.<sup>32,42</sup> Spherical white contrast areas were observed in thin regions of the garnet sample after irradiation with cluster ions (10–40 MeV  $\text{C}_{60}$ ), but could never be observed after monoatomic ion irradiation. Therefore, it is likely that the creation of the areas of white contrast, presumably corresponding to areas of lower density, inside damage tracks is a general phenomenon originating from the very high density of energy deposited in poorly conducting materials. The level of excitation is so high that the resulting pressure can indeed eject material from the center of the track as long as the surfaces are not too far away.

## §4. Magneto-optical imaging of the flux distribution in the superconducting mixed state

### 4.1 Experimental procedure

The critical current density and magnetic relaxation experiments were carried out using Magneto-Optical Imaging<sup>44</sup> at temperatures between 20 and 60 K, and inductions up to  $H_{max} = 700$  G. In this technique, a 4  $\mu\text{m}$ -thick ferrimagnetic garnet indicator film with in-plane anisotropy, covered by an Al mirror, is placed on the  $\text{Bi}_2\text{Sr}_2\text{CaCu}_2\text{O}_{8+\delta}$  crystal surface. Linearly polarized light is transmitted through the garnet, reflected on the Al mirror, and transmitted through the garnet a second time. The Faraday rotation of the light’s polarization vector, which is proportional to the perpendicular component of the garnet magnetization, and to the local induction at the  $\text{Bi}_2\text{Sr}_2\text{CaCu}_2\text{O}_{8+\delta}$  crystal surface, is observed using a nearly crossed analyzer. The resulting image, recorded using a polarized light microscope and a



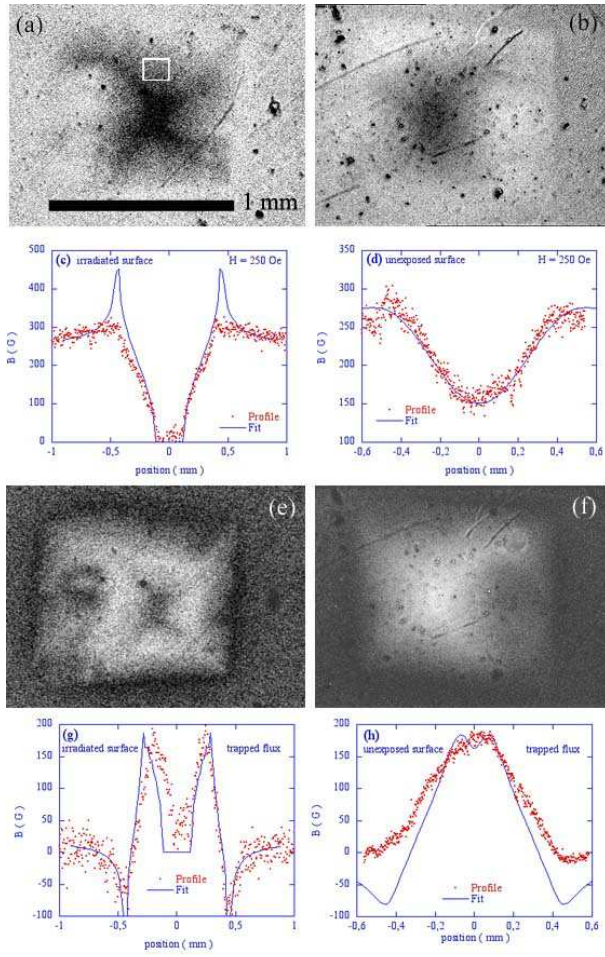


Fig. 7. Magneto-optical images of the magnetic induction on the surface of the  $\text{Bi}_2\text{Sr}_2\text{CaCu}_2\text{O}_{8+\delta}$  crystal, after irradiation with 30 MeV  $C_{60}$ . The images show the flux density on the crystal surface that was exposed to the molecular beam (a,e), as well as on the unexposed surface (b,f). (a,b) Flux penetration at 45.6 K, after zero-field cooling and the application of an external field,  $H_a = 250$  Oe. The small rectangle denotes the area in which the data of fig. 8 were obtained. (c,d) Flux profiles taken from the top to the bottom of images (a) and (b), respectively, through the crystal center. Drawn lines show the flux profile expected from the critical state model,<sup>46)</sup> supposing that the critical current of  $1.6 \times 10^{11} \text{ Am}^{-2}$  flows only in the 200 nm-thick top layer containing the columnar tracks induced by the  $C_{60}$ -irradiation; (c) at  $1 \mu\text{m}$  above the surface (d) at  $60 \mu\text{m}$  from the irradiated surface. (e,f) Trapped flux after removal of a maximum applied field of 320 Oe (e) and 580 Oe (f). (g) and (h) remanent flux profiles expected from the critical state, at  $1 \mu\text{m}$  above the surface (g) and at  $60 \mu\text{m}$  from the irradiated surface (h).

CCD camera, reveals the modulation of the perpendicular ( $z$ ) component of the local induction at the sample surface as intensity differences.

Figure 7(a) shows an image of the irradiated crystal after zero-field cooling to 45.6 K and the application of a 250 Oe external field. The indicator film was placed

directly on the irradiated surface. Bright areas reflect a high local induction, while dark areas have small local induction. All images were calibrated using the light intensity measured far from the sample during a field sweep. Figure 7(a) clearly shows a flux density distribution that

is characteristic of the Bean model and strong flux pinning,<sup>45–48)</sup> at a temperature and field at which unirradiated crystals show no bulk flux pinning.<sup>49,50)</sup> Figure 7(c) shows a flux profile, taken from the top to the bottom of fig. 7(a), through the crystal center. The flux profile is compared to that expected over a thin strip sample of width  $w$  and thickness  $d$  in the critical state. This is obtained by applying the Biot-Savart law to the current density distribution derived in ref.,<sup>46)</sup>

$$j = j_c \quad (x_f < |x| < w)$$

$$j = \frac{2}{\pi} j_c \arctan Q \quad (0 < |x| < x_f)$$

where  $Q = x[1 - (x_f/d)^2]^{1/2}(x_f^2 - x^2)^{-1/2}$ ,  $H_a$  is the applied field, and

$$x_f = \frac{w}{2} \frac{1}{\cosh(\pi H_a / j d)} \quad (1)$$

is the position of the flux front. Good agreement is obtained if we assume that the indicator is separated from the sample by a distance of  $1 \mu\text{m}$ , and that a (field-independent) critical screening current of  $1.6 \times 10^{11} \text{ Am}^{-2}$  flows only in the top 200 nm of the crystal. This layer corresponds to that which contains the tracks created by the  $C_{60}$ -irradiation. Figure 7(e) shows the trapped flux on the irradiated crystal surface after removal of the applied field. In this case, good agreement is again obtained by assuming that the critical current flows only in the layer containing the tracks, and applying the rule  $B(x, H_a) = B(x, H_{max}) - 2B(x, \frac{1}{2}H_{max} - \frac{1}{2}H_a)$  applicable following a reversal of the field sweep direction. In contrast, images collected with the magneto-optical indicator film placed on the opposite surface, that remained unexposed to the  $C_{60}$  beam, show much smoother, shallower flux profiles. These show that a large distance, exceeding the sample thickness, separates the current-carrying layer containing the tracks from the indicator surface. Thus, we surmise that the critical current flows mainly in the 200 nm thick layer containing the tracks,

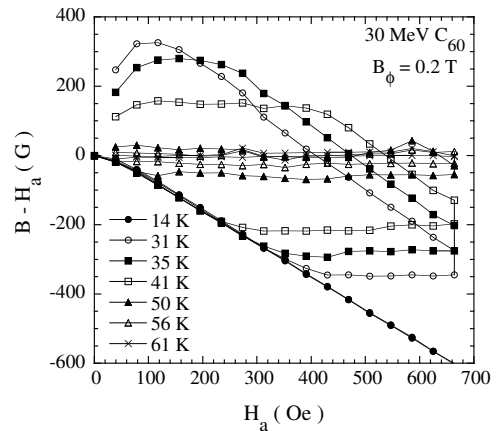


Fig. 8. Hysteresis of the “self-field”, defined as the difference between the local induction  $B$  and the applied field  $H_a$ , averaged on the square region of the  $C_{60}$ -irradiated  $\text{Bi}_2\text{Sr}_2\text{CaCu}_2\text{O}_{8+\delta}$  crystal outlined in fig. 7. Data are for images taken on the irradiated surface.

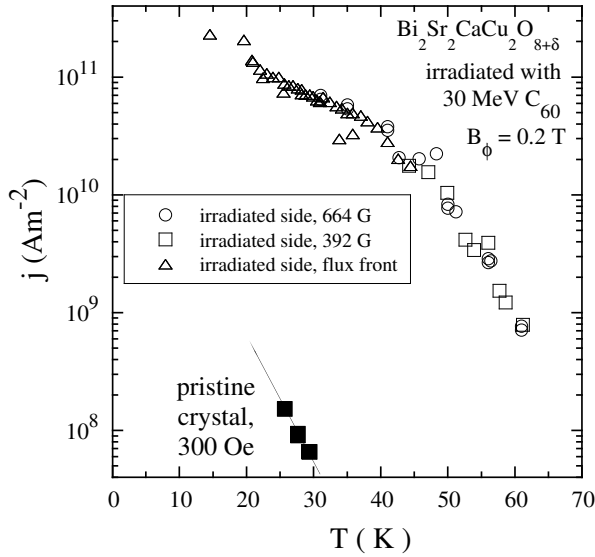


Fig. 9. Sustainable current density, at  $E = 6 \mu\text{Vm}^{-1}$ , of the  $\text{C}_{60}$ -irradiated  $\text{Bi}_2\text{Sr}_2\text{CaCu}_2\text{O}_{8+\delta}$  single crystal. The (field-independent) current was measured from magneto-optical images of the flux distribution on the irradiated surface. Induction values are 664 G ( $\circ$ ), 392 G ( $\square$ ), and 0 (position of the flux-front) ( $\triangle$ ). Filled squares joined by a drawn line represent data on the crystal prior to irradiation.

and that all screening in the rest of the crystal is produced by this current only.

#### 4.2 Determination of the critical current density

Magnetic hysteresis loops of the local induction were recorded by sweeping the external field at a rate of 120 Oe/s, corresponding to an induced electric field at the crystal edge,  $E = 6 \mu\text{Vm}^{-1}$ . This was achieved by controlling the bipolar power supply output with a 0.1 Hz triangular wave. A synchronized TTL signal triggered image acquisition at the rate of 4 images / s. For these experiments, the polarizer/ analyzer pair of the microscope was uncrossed by  $10^\circ$ . After conversion of the image intensity to flux density, hysteresis loops of the local induction  $B(H_a)$  were determined in several points on the crystal surface. Subtraction of the applied field yielded hysteresis loops of the crystal “self-field”  $B - H_a$ , such as depicted in fig. 8. The sustainable current density was obtained from the critical state model.<sup>46–48</sup> At fields above the full penetration field  $H_p$  (at which the flux front has penetrated to the center of the crystal) and less than  $H_{max} - H_p$  (at which the remagnetization front has reached the crystal center), the width  $\Delta(B - H_a)$  of the hysteresis loops, which is proportional to the sustainable current density  $j$ , turns out to be field-independent. The absolute magnitude of the current density was verified using the relation (1) between applied field and the position of the flux front,<sup>46</sup> taking the crystal width  $w = 800 \mu\text{m}$  and  $d = 200 \text{ nm}$ , the thickness of the surface layer containing continuous latent tracks. In this manner, we obtained the temperature dependence of  $j$  on the irradiated surface, between 20 and 60 K, for inductions up to 664 G (fig. 9).

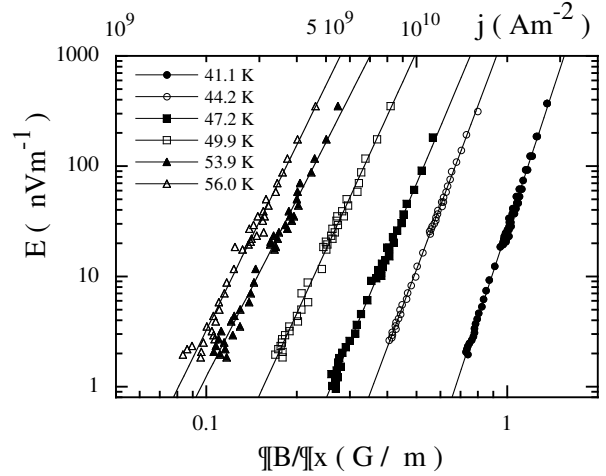


Fig. 10. Power-law  $I(V)$ -characteristics, measured by magneto-optical imaging of the relaxation of the non-equilibrium magnetic induction distribution on the  $\text{C}_{60}$ -irradiated surface of the  $\text{Bi}_2\text{Sr}_2\text{CaCu}_2\text{O}_{8+\delta}$  single crystal.

#### 4.3 Magnetic relaxation and $I(V)$ -curves

Experiments on the temporal relaxation of the distribution of trapped flux were prepared by zero-field cooling to the working temperature and applying a field of 650 Oe. A two-channel synthesizer was used to simultaneously trigger the decrease of the applied field to 50 Oe, and the acquisition of magneto-optical images of the trapped flux. Images were acquired between 1 s and 200 s after reaching the 50 Oe target field. The flux distributions always corresponded to the Bean critical state profile, in accordance with a strongly nonlinear  $I(V)$ -characteristic. From the relaxing profiles, we obtained the current density as the induction gradient,  $j = -\partial B_z / \partial x$ , and the electric field as  $E = \int_0^{w/2} (\partial B / \partial t) dx$ .<sup>51</sup> The electric field was verified to decay as  $E \propto 1/t$ .<sup>52</sup> The process was repeated for a number of temperatures at which full flux penetration could be achieved, with images taken both on the irradiated and on the unirradiated side of the crystal. Resulting  $I(V)$ -curves are displayed in fig. 10. The  $I(V)$ -curves follow a power-law at all investigated temperatures. The long-time behavior of the electric field at the sample edge, which for the measured power-law  $I(V)$ -relation follows  $E(w/2) = \frac{1}{4} \mu_0 j_c w^2 (\tau_0 + t)^{-1}$ , with  $\tau_0 \approx 10 \text{ ms}$  a transient time, allows an estimate of the “true” critical current density  $j_c = t \times [4E(w/2, t \gg \tau_0) / \mu_0 w^2]$ . This was found to coincide, within experimental error, with the data points of fig. 9.

#### 4.4 Determination of the Phase Diagram

Differential Magneto-Optical Imaging<sup>53,54</sup> was used to determine the  $(B, T)$  phase diagram. After stabilization of the temperature, ten magneto-optical images are acquired at the target applied field  $H_a$ , and averaged. The magnetic field is then increased by  $\Delta H_a = 0.5 \text{ Oe}$ , whence ten new images are acquired and consecutively subtracted from the initial average, to yield a differential

image. The process is repeated twenty times to increase the signal-to-noise ratio. The result is an image of the “local permeability”,  $\Delta B/\Delta H_a$  (see fig. 11). Areas of  $\Delta B/\Delta H_a = 1$ , such as the space surrounding the crystal, would show up as grey (not shown in fig. 11 that displays only the surface within the crystal perimeter). Regions that show diamagnetic screening, such as the crystal center in fig. 11(a), are revealed as black. Areas that, in the field interval between  $H_a$  and  $H_a + \Delta H_a$ , undergo the phase change from vortex solid to vortex liquid, experience an increase  $\Delta B_{FOT}$  in the equilibrium flux (vortex) density and thus have positive permeability.<sup>53,55</sup> Therefore, the clear white areas show the progression of the phase transformation front in the field interval ( $H_a$ ,  $H_a + \Delta H_a$ ). The magnitude of the equilibrium flux density change  $\Delta B_{FOT}$  is plotted versus temperature in the Inset of fig. 12. Figure 11 shows a series of images at 82.0 K, as the applied field is increased from 26 Oe to 31 Oe in 1 Oe steps. One sees that the vortex liquid nucleates in a number of spots in the upper left hand corner, rapidly expands, and finally occupies the whole crystal, except for a narrow ring around the crystal outer edge.

From the DMO images, we determine the phase diagram of the  $C_{60}$ -irradiated  $\text{Bi}_2\text{Sr}_2\text{CaCu}_2\text{O}_{8+\delta}$  single crystal. The field of first flux penetration corresponds to the applied field at which a non-zero flux can be observed at any spot in the crystal. The FOT field is determined, for a given spot on the crystal surface, as the applied field at which the modulation  $\Delta H_a$  produces a paramagnetic signal (white in fig. 11) at that location. The local irreversibility line (IRL), or  $H_{irr}(T)$  line at which the critical current density vanishes, is determined as the applied field at which the image intensity in a given spot coincides with the intensity caused by the full 0.5 Oe field modulation. Both the FOT line and the IRL depend on position, because of field inhomogeneity caused by both sample geometry and composition. The spread of  $H_{FOT}$  and  $H_{irr}$  is denoted by the error bars in fig. 12. It is remarkable that, for high temperatures, the vortex solid undergoes the transition to the vortex liquid in the peripheral crystal areas of high local induction [white stripes near the crystal boundary in fig. 11 (a,b)], while in the vortex solid near the crystal center vortices are still pinned and the field modulation is completely screened [black spots near the crystal boundary in fig. 11 (a,b)]. Similar behavior was recently observed in inhomogeneous underdoped  $\text{Bi}_2\text{Sr}_2\text{CaCu}_2\text{O}_{8+\delta}$  crystals.<sup>56</sup> Below 74 K, the equilibrium flux density change associated with the FOT becomes indistinguishable from the demagnetizing field due to strong screening currents in the sample center. Therefore, the FOT line is not plotted below this temperature.

## §5. Discussion

The  $(B, T)$  phase diagram of the  $C_{60}$  irradiated  $\text{Bi}_2\text{Sr}_2\text{CaCu}_2\text{O}_{8+\delta}$  crystal surprisingly features *both* the FOT normally observed only in pristine<sup>6</sup>) or very lightly irradiated<sup>3</sup>) single crystals, *as well as* the exponential irreversibility line associated with the Bose-glass to vor-

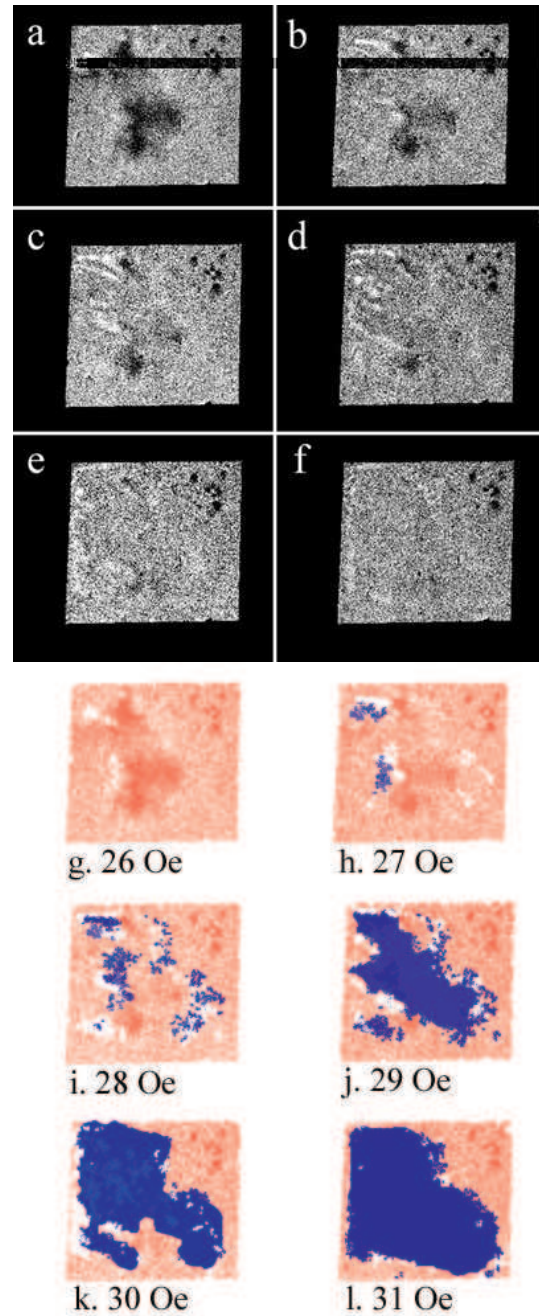


Fig. 11. Differential magneto-optical (DMO) images of the first order vortex phase transition in an optimally doped  $\text{Bi}_2\text{Sr}_2\text{CaCu}_2\text{O}_{8+\delta}$  single crystal irradiated with 30 MeV  $C_{60}$  fullerenes. The frames follow the crystal outline. The images were taken at  $T = 82.0$  K, in applied magnetic fields of 26 (a) to 31 Oe (f), each image corresponding to a 1 Oe step. The field modulation  $\Delta H_a$  was 0.5 Oe. Dark areas show diamagnetic screening, while white areas show the paramagnetic response due to the progression of the phase transformation front. (g)-(l) Interpretation of images (a)-(f) in terms of the growth of the vortex liquid phase (blue) at the expense of the vortex solid (red).

tex liquid transition in heavy-ion irradiated samples.<sup>20</sup> Moreover, the two transitions occur at *exactly the same locations* as in pristine and heavy-ion irradiated crystals, respectively.<sup>6,20</sup> By virtue of their larger diameter  $D = 20$  nm, one would expect the vortex pinning energy per unit length of the latent tracks created by the  $C_{60}$  fragments,  $U_p \approx \varepsilon_0(D/2\xi)^2$  to be one order of magnitude

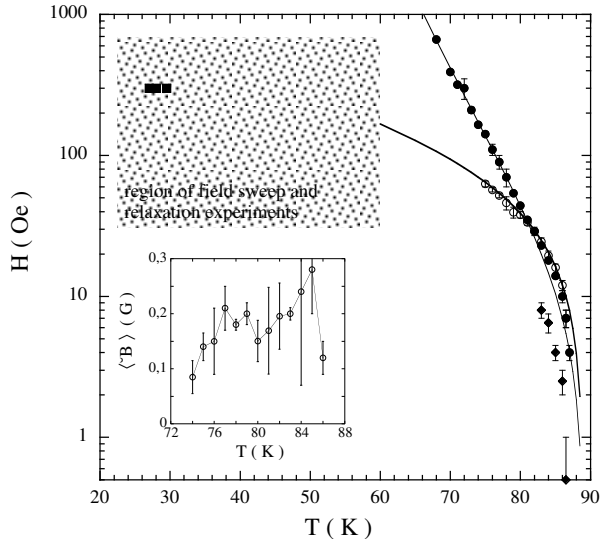


Fig. 12. Phase diagram of single crystal  $\text{Bi}_2\text{Sr}_2\text{CaCu}_2\text{O}_{8+\delta}$  irradiated with 30 MeV  $\text{C}_{60}$  fullerenes. Symbols denote the field of first flux penetration ( $\diamond$ ), the First Order Transition field  $H_{FOT}$  ( $\circ$ ), and the irreversibility field  $H_{irr}$  ( $\bullet$ ) after  $\text{C}_{60}$  irradiation. The filled squares denote the field of the “second-peak” transition, or low temperature part of the FOT, in the pristine crystal.<sup>10, 58</sup> Error bars denote the spread of FOT fields within the crystal. The drawn line through the FOT data is a guide to the eye, the drawn line through the  $H_{irr}$  data is a fit to eq. (2) with parameters  $B_{cr} = 70$  G and  $\varepsilon_0(0)s/k_B = 770$  K. Inset: magnitude of the equilibrium change in flux density at the FOT,  $\Delta B_{FOT}$ . The error bars show the spread of  $\Delta B_{FOT}$  within the sample.

larger than that of tracks created by swift heavy ions, with  $D = 7$  nm.<sup>57</sup> Here  $\varepsilon_0(T) = \Phi_0^2/4\pi\mu_0\lambda_{ab}^2(T)$  is the typical vortex energy,  $\lambda_{ab}(T)$  is the in-plane penetration depth, and  $\xi$  is the coherence length. We conclude that the irreversibility line in layered superconductors containing columnar tracks is not influenced by the pinning energy of the defect.

We now discuss the simultaneous observation of the FOT and the exponential glass-to-liquid irreversibility line. Plausibly, the latter line is determined only by the outer layer containing the latent tracks, while the FOT occurs only in the rest of the crystal. The large screening current in the irradiated layer of the crystal is sufficiently strong to prevent flux penetration throughout the crystal, one can therefore observe its effects up to the irreversibility line on both crystal surfaces. As for the FOT, one might naively expect that this occurs only in the ordered Bragg glass, but not in the strongly pinned “top” part of the vortex ensemble that occupies the latent tracks. Recent measurements by Banerjee *et al.* have shown that the FOT persists in crystals with a modest track density,  $n_d < 5 \times 10^8 \text{ cm}^{-2}$  or  $B_\phi \leq 100$  G, even though the vortex solid in such crystals is completely disordered.<sup>3, 11</sup> Here, we report the unprecedented observation of the FOT of the vortex solid in the presence of a track density  $n_d = 1 \times 10^{10} \text{ cm}^{-2}$ , or  $B_\phi = 0.2$  T. One possibility is that the vortex FOT is occurring only in the defect-free part of the crystal, and that the vortex density change at the FOT is propagated in the

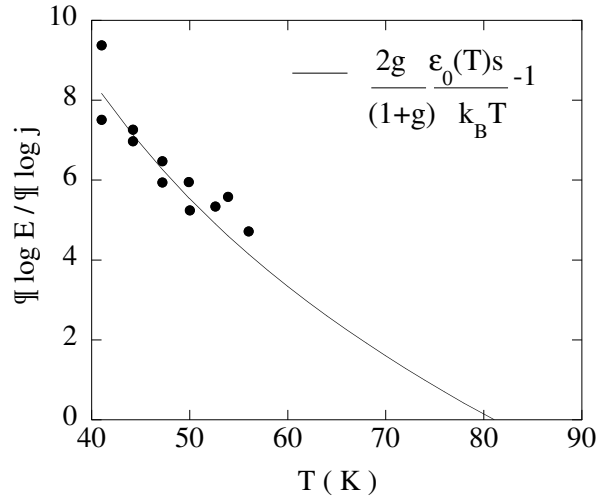


Fig. 13. Logarithmic slope  $\partial \log E / \partial \log j$  of the current-voltage characteristics of the  $\text{C}_{60}$ -irradiated  $\text{Bi}_2\text{Sr}_2\text{CaCu}_2\text{O}_{8+\delta}$  single crystal. The drawn line corresponds to the Coulomb gas<sup>62</sup> prediction  $2(g/1+g)\varepsilon_0(T)s/k_B T - 1$  (with  $\varepsilon_0(0)s/k_B = 770$  K, and  $g = 0.4$ ).

pinned upper portion of the vortex ensemble. It would imply that above 74 K, the lowest temperature at which we unambiguously observe the FOT, the sustainable current density is smaller than the  $1.6 \times 10^6 \text{ Am}^{-2}$  needed to screen  $\Delta B_{FOT}$ . An extrapolation of the high temperature part of the  $j(T)$ -curve of fig. 9 shows that, in spite of its very fast temporal relaxation, the screening current at 74 K is still more than an order or magnitude larger than this. Thus, in spite of the presence of very strong pinning centers, the vortex system still seems to undergo the FOT in the high temperature part of the phase diagram.

We now turn to the nature of the high-field vortex state, at fields higher than  $H_{FOT}$ . Figure 12 shows that, at least in the layer containing latent tracks, a very considerable portion of the vortex liquid (the region above the FOT line, without critical current before irradiation) is transformed to a pinned state of localized vortices, with a very high critical current density (fig. 9). A framework that provides a conceptual language by which the behavior in the high field vortex state can be understood is the vacancy interstitial-unbinding transition of the 2D pancake vortex lattices contained within each superconducting layer. This transition is of Kosterlitz-Thouless type.<sup>59, 60</sup> In a clean layered superconductor, the energy to create a vacancy-interstitial (dislocation quartet) in the pancake vortex lattice is non-zero only because of the non-zero interlayer coupling, which provides an effective “substrate potential” for the vortices. For weak (electromagnetic) coupling, it means the unbinding transition lies at a rather low temperature,  $T \approx (g/1+g)\varepsilon_0s/2k_B$   $s = 1.5$  nm is the  $\text{CuO}_2$  layer spacing.<sup>60</sup> The factor  $g$  describes the relative weight of in-plane- to interlayer pancake vortex interactions: if the first dominate,  $g \ll 1$ , if the interlayer coupling is important,  $g > 1$ .<sup>60</sup> In Ref.,<sup>20</sup> it was implicitly supposed that



the introduction of columnar defects by heavy-ion irradiation effectively enhances  $g$ , by two mechanisms (i) the localization of vortices on the tracks prevents the elastic screening of a vortex-lattice vacancy or interstitial (ii) the columns may artificially enhance the interlayer coupling by aligning the pancakes. The consequence is that the defect-pair energy is close to  $\varepsilon_0 s$ , and that the irreversibility line, which is supposed to coincide with the vacancy–interstitial unbinding transition, does not depend on details of the pinning potential.

Henceforth, the irreversibility line was estimated as<sup>20,59)</sup>

$$B_{irr} = B_{cr} \frac{\varepsilon_0(T)s}{k_B T} \exp \left[ \frac{\varepsilon_0(T)s}{k_B T} \right], \quad (2)$$

with  $B_{cr} \equiv \Phi_0/(\gamma s)^2$  the crossover field,<sup>59,60)</sup>  $\gamma s$  the Josephson length, and  $\gamma$  the anisotropy parameter. Equation (2) very well describes the irreversibility (Bose-glass) line in heavy-ion irradiated Bi<sub>2</sub>Sr<sub>2</sub>CaCu<sub>2</sub>O<sub>8+ $\delta$</sub>  of different doping levels.<sup>20)</sup> Figure 12 shows that such a comparison holds equally well for C<sub>60</sub>-irradiated Bi<sub>2</sub>Sr<sub>2</sub>CaCu<sub>2</sub>O<sub>8+ $\delta$</sub> . The fit to the irreversibility line yields  $B_{cr} = 70$  G and  $\varepsilon_0(0)s/k_B = 770$  K, consistent with  $\lambda_{ab}(0) = 185$  nm (*i.e.* a London penetration depth  $\lambda_L(0) = 250$  nm) and  $\gamma = 360$ . These are the literature values for optimally doped Bi<sub>2</sub>Sr<sub>2</sub>CaCu<sub>2</sub>O<sub>8+ $\delta$</sub> .<sup>61)</sup> Thus, the transition from pinned vortex state to vortex liquid in C<sub>60</sub>-irradiated Bi<sub>2</sub>Sr<sub>2</sub>CaCu<sub>2</sub>O<sub>8+ $\delta$</sub>  bears all the hallmarks of the proposed vortex-unbinding transition: it obeys eq. (2) and is independent of the pinning potential.

In case the high-field vortex solid-liquid transition is indeed the defect-unbinding transition, one ought to expect power-law  $I(V)$  curves in the solid,  $E \propto j^a$ . Here, the power  $a = (g/1 + g)2\varepsilon_0(T)s/k_B T - 1$  is determined by the effective Coulomb gas “charge”  $[2(g/1 + g)\varepsilon_0 s]^{1/2}$ .<sup>62)</sup> Note that  $g$  and therefore  $a$  are, in principle, field-dependent; the exponential behavior of the irreversibility line suggests  $a \propto 1/\ln(B/B_{cr})$ . Figure 10 shows that the  $I(V)$ -curves at intermediate temperature indeed follow a power-law. The power  $\partial \log E / \partial \log j$  is plotted in fig. 13. A comparison with the magnitude and temperature dependence expected for  $\varepsilon_0(0)s/k_B = 770$  K found previously yields reasonable agreement if one sets  $g/1 + g \approx 0.3$ , *i.e.*  $g \approx 0.4$ . This value, although highly approximate ( $g$  is expected to depend on field and temperature) suggests that intra-layer pancake vortex interactions and the lack of elastic relaxation of the pinned lattice is what determines both the dynamics and the vortex phase diagram.

## §6. Conclusions

We have produced large diameter (20  $\mu$ m) short (200 nm) damage tracks on a single surface of a Bi<sub>2</sub>Sr<sub>2</sub>CaCu<sub>2</sub>O<sub>8+ $\delta$</sub>  single crystal by 30 MeV C<sub>60</sub> irradiation. After the irradiation, the vortex matter still shows the first order transition found in pristine crystal, but also the exponential irreversibility line normally found in heavy-ion irradiated Bi<sub>2</sub>Sr<sub>2</sub>CaCu<sub>2</sub>O<sub>8+ $\delta$</sub> . Measurements of the flux distribution, magnetic relaxation, and  $I(V)$ -curves demonstrate exceptionally strong flux pinning. However, quantitative analysis of the data shows

that neither the sustainable current density, nor the irreversibility line, depend on the pinning potential of the columnar tracks. More specifically, we suggest that the increase in current density after irradiation is due to the increase of the energy of a vacancy-interstitial pair in the pancake vortex lattice in each layer.

## Acknowledgments

We are grateful to Y. Mehtar-Tani for the measurements on the pristine crystal.

- 
- 1) M. Konczykowski, F. Rullier-Albenque, E.R. Yacoby, A. Shaulov, Y. Yeshurun, and P. Lejay, Phys. Rev. B **44** (1991) p.7167.
  - 2) M. Konczykowski, Y. Yeshurun, L. Klein, E.R. Yacoby, N. Chikumoto, V.M. Vinokur, and M.V. Feigel'man, J. Alloys Comp. **195** (1993) p.407.
  - 3) S. S. Banerjee, A. Soibel, Y. Myasoedov, M. Rappaport, E. Zeldov, M. Menghini, Y. Fasano, F. de la Cruz, C. J. van der Beek, M. Konczykowski, and T. Tamegai, Phys. Rev. Lett. **90**(2003) p.087004.
  - 4) C. Dasgupta and O. T. Valls, Phys. Rev. B **66** (2002) p.064518.
  - 5) C. Dasgupta and O. T. Valls, Phys. Rev. Lett. **91** (2003) p.127002.
  - 6) E. Zeldov, D. Majer, M. Konczykowski, V.B. Geshkenbein, V.M. Vinokur, and H. Strikman, Nature **375** (1995) p.373.
  - 7) T. Giamarchi and P. LeDoussal, Phys. Rev. Lett. **76** (1996) p.3408.
  - 8) D. Fuchs, R.A. Doyle, E. Zeldov, D. Majer, W.S. Seow, R.J. Drost, T. Tamegai, S. Ooi, M. Konczykowski, and P.H. Kes, Phys. Rev. B **55** (1997) p.R6156.
  - 9) D. T. Fuchs, R. A. Doyle, E. Zeldov, S. F. W. R. Rycroft, T. Tamegai, S. Ooi, M. L. Rappaport, and Y. Myasoedov, Phys. Rev. Lett. **81** (1998) p.3944.
  - 10) C.J. van der Beek, S. Colson, Y. Mehtar-Tani, to be published.
  - 11) M. Menghini, Yanina Fasano, F. de la Cruz, S.S. Banerjee, Y. Myasoedov, E. Zeldov, C. J. van der Beek, M. Konczykowski, and T. Tamegai, Phys. Rev. Lett. **90** (2003) p.147001.
  - 12) S. Colson, M. Konczykowski, M. B. Gaifullin, Y. Matsuda, P. Gierlowski, M. Li, P. H. Kes, and C. J. van der Beek, Phys. Rev. Lett. **90** (2003) p.137002.
  - 13) C.J. van der Beek, M. Konczykowski, V.M. Vinokur, T.W. Li, P.H. Kes, and G.W. Crabtree, Phys. Rev. Lett. **74** (1995) p.1214.
  - 14) R. Doyle, W.S. Seow, Y. Yan, A.M. Campbell, T. Mochiku, K. Kadowaki, and G. Wirth, Phys. Rev. Lett. **77** (1996) p.1155.
  - 15) D. López, E.F. Righi, G. Nieva, F. de la Cruz, W.K. Kwok, J.A. Fendrich, G.W. Crabtree, and L. Paulius, Phys. Rev. B **53** (1996) p.R8895.
  - 16) M. Kosugi, Y. Matsuda, M.B. Gaifullin, L.N. Bulaevskii, N. Chikumoto, M. Konczykowski, J. Shimoyama, K. Kishio, K. Hirata, and K. Kumagai, Phys. Rev. Lett. **79**(1997) p.3763.
  - 17) M. Sato, T. Shibauchi, S. Ooi, T. Tamegai, and M. Konczykowski, Phys. Rev. Lett. **79** (1997) p.3759.
  - 18) S. Colson, C.J. van der Beek, M. Konczykowski, M. Gaifullin, Y. Matsuda, P. Gierlowski, Ming Li, and P.H. Kes, condmat/0401281.
  - 19) S.S. Banerjee *et al.*, to be published (2004)
  - 20) C.J. van der Beek, M. Konczykowski, A.V. Samoilov, N. Chikumoto, and M.V. Feigel'man, Phys. Rev. Lett. **86** (2001) p.5136.
  - 21) D.R. Nelson and V.M. Vinokur, Phys. Rev. Lett. **68** (1992) p.2398; D.R. Nelson and V.M. Vinokur, Phys. Rev. B **48**(1993) p.13060.
  - 22) A.I. Larkin and V. M. Vinokur, Phys. Rev. Lett. **75** (1995) 4666.
  - 23) Y. Fasano, M. de Seta, M. Menghini, H. Pastoriza, and F. de la Cruz, Solid State Communications **128** (2003) p.51.

- 24) B. Khaykovich, D. T. Fuchs, K. Teitelbaum, Y. Myasoedov, E. Zeldov, T. Tamegai, S. Ooi, M. Konczykowski, R. A. Doyle, and S. F. W. R. Rycroft, *Phys. Rev.* **61** (2000) p.R9261.
- 25) Ming Li, C.J. van der Beek, M. Konczykowski, A.A. Menovsky, and P.H. Kes, *Phys. Rev. B* **66** (2002) p.024502.
- 26) B. Khaykovich, E. Zeldov, D. Majer, T.W. Li, P.H. Kes, and M. Konczykowski, *Phys. Rev. Lett.* **76**(1996) p.2555.
- 27) J.P. Biersack, and L.G. Haggmark, *Nucl. Instr. and Meth.* **174** (1980) p.257.
- 28) K. Baudin, A. Brunelle, M. Chabot, S. Della-Negra, J. Depauw, D. Gardes, P. Hakansson, Y. Le Beyec, A. Billebaud, M. Fallavier, J. Remillieux, J.C. Poizat, and J.P. Thomas, *Nucl. Instr. and Meth. B* **94** (1994) p.341.
- 29) C. Tomaschko, D. Brandl, R. Krger, M. Schurr, and H. Voit, *Nucl. Instr. and Meth. B* **103** (1995) p.407.
- 30) D. Ben-Hamu, A. Baer, H. Feldman, J. Levin, O. Heber, Z. Amitay, Z. Vager, and D. Zajfman, *Phys. Rev. A* **56** (1997) p. 4786.
- 31) A. Dunlop, G. Jaskierowicz, J. Jensen, and S. Della-Negra, *Nucl. Instr. and Meth.* **132** (1997), p.93.
- 32) J. Jensen, A. Dunlop, S. Della-Negra, and H. Pascard, *Nucl. Instr. and Meth. B* **135** (1998) p.295.
- 33) L. Reimer, in *Transmission electron microscopy* , Springer, 1997, p. 198.
- 34) D. B. Williams, C. B. Carter, in *Transmission Electron Microscopy* , Plenum Press, New-York, 1996, p. 357.
- 35) J. Wiesner, C. Træholt, J.-G. Wen, H.-W. Zandbergen, G. Wirth, and H. Fuess, *Physica C* **268** (1996) p. 161.
- 36) M. Sasase, S. Okayasu, H. Kurata, and K. Hojou, *Physica C* **357-360** (2001) p.497.
- 37) Y. Zhu, Z.X. Cai, R.C. Budhani, M. Suenaga, and D.O. Welch, *Phys. Rev. B* **48** (1993) p.6436.
- 38) N.Kuroda, N. Ishikawa, Y. Chimi, A. Iwase, H. Ikeda, R. Yoshizaki, and T. Kambara, *Phys. Rev. B* **63** (2001) p.224502.
- 39) D. X. Huang, Y. Sasaki and Y. Ikuhara, *Phys. Rev. B* **59** (1999) p.3862.
- 40) D. X. Huang, Y. Sasaki, I. Hirabayashi and Y. Ikuhara, *Phys. Rev. B* **61** (2000) p.15442.
- 41) A. Meftah, F. Brisard, J.M. Costantini, M. Hage-Ali, J.P. Stoquert, F. Studer, and M. Toulemonde, *Phys. Rev. B* **48** (1993) p.920.
- 42) J. Jensen, A. Dunlop, S. Della-Negra, and M. Toulemonde, *Nucl. Instr. and Meth. B* **146** (1998) p.412.
- 43) Z.G. Wang, Ch. Dufour, B. Cabeau, J. Dural, G. Fuchs, E. Paumier, F. Pawlak, and M. Toulemonde, *Nucl. Instrum. Meth. B* **107** (1996) p.175.
- 44) L.A. Dorosinskiĭ, M.V.Indenbom, V.I. Nikitenko, Yu.A. Ossip'yan, A.A. Polyanskii, and V.K. Vlasko-Vlasov, *Physica C* **203** (1992) p.149.
- 45) C.P. Bean, *Phys. Rev. Lett.* **8** (1962) p.250.
- 46) E.H. Brandt, M.V. Indenbom, and A. Forkl, *Europhys. Lett.* **22** (1993) p.735.
- 47) E. Zeldov, J.R. Clem, M. McElfresh, and M. Darwin, *Phys. Rev. B* **49** (1994) p.9802.
- 48) E.H. Brandt, *Phys. Rev. B* **54** (1996) p.4246 .
- 49) M.V. Indenbom, *Physica (Amsterdam) C* **235-240**(1994) p.201.
- 50) E. Zeldov, A.I. Larkin, V.B. Geshkenbein, M.Konczykowski, D. Majer, B. Khaykovich, V.M. Vinokur, and H.Strikhman, *Phys. Rev. Lett.* **73** (1994) p.1428.
- 51) Y. Abulafia, A. Shaulov, Y. Wolfus, R. Prozorov, L. Burlachkov, Y. Yeshurun, D. Majer, E. Zeldov, and V. M. Vinokur, *Phys. Rev. Lett.* **75**(1995) p.2404.
- 52) A. Gurevich and E.H. Brandt, *Phys. Rev. Lett.* **73** (1994) p.178.
- 53) A. Soibel, E. Zeldov, M. Rappaport, Y. Myasoedov, T. Tamegai, S. Ooi, M. Konczykowski, et V. Geshkenbein, *Nature* **406** (2000) p.282.
- 54) A. Soibel, Y. Myasoedov, M.L. Rappaport, T. Tamegai, S.S. Banerjee, and E. Zeldov, *Phys. Rev. Lett.* **87** (2001) p.167001.
- 55) N. Morozov, E. Zeldov, D. Majer and M. Konczykowski, *Phys. Rev. B* **54** (1996) p.R3784.
- 56) C.J. van der Beek, I. Abalosheva, M. Konczykowski, Ming Li, P.H. Kes, and M.V. Indenbom, in *Magneto-Optical Imaging* , ed. T.H. Johansen and D.V. Shantsev, NATO Science Series, Kluwer Academic Publishers, (in press).
- 57) R.J. Drost, C.J. van der Beek, H.W. Zandbergen, M. Konczykowski, A.A. Menovsky, and P.H. Kes, *Phys. Rev. B* **60** (1999) p.13612.
- 58) N. Avraham, B. Khaykovich, Y. Myasoedov, M. Rappaport, H. Shtrikman, D.E. Feldman, T. Tamegai, P.H. Kes, Ming Li, M. Konczykowski, C.J. van der Beek, and E. Zeldov, *Nature* **411** (2001) p.451.
- 59) M.V. Feigel'man, V.B. Geshkenbein, and A.I. Larkin, *Physica C* **167** (1990) p. 117.
- 60) M.J.W. Dodgson, V.B. Geshkenbein, and G. Blatter, *Phys. Rev. Lett.* **83** (1999) p.5358.
- 61) T.W. Li, R.J. Drost , P.H. Kes, C. Træholt, H.W. Zandbergen, N.T. Hien, A.A. Menovsky, and J.J.M. Franse, *Physica C* **274** (1997) p.197.
- 62) P. Minnhagen, O. Westman, A. Jonsson, and P. Olsson, *Phys. Rev. Lett.* **74** (1995) p.3672.